THE ASTROPHYSICAL JOURNAL, 397:174–186, 1992 September 20

THE UNUSUAL COMETARY STAR-FORMING REGION G110−13

STEN ODENWALD,[1,2] JACQUELINE FISCHER,[2] FELIX J. LOCKMAN,[3] AND SALLY STEMWEDEL[2,4]
Received 1990 September 21; accepted 1992 March 30

ABSTRACT

We present far-IR, radio continuum, and spectral line observations of an unusual, highly elongated, comet-shaped molecular cloud, located ∼100 pc from the Galactic plane. The presence of three late B-type stars embedded within, or adjacent to, this low-mass (≈60 $M_\odot$) cloud implies a star-forming efficiency that may be as high as 30%. Several mechanisms that may have been responsible for its unusual morphology and high star-forming efficiency will be described and evaluated. Although ram-pressure resulting from the rapid motion of this cloud through the interstellar medium could explain its streamlined appearance, there is evidence that G110−13 is the compression front formed by a recent cloud collision.

Subject headings: ISM: clouds — ISM: individual (G110−13)

1. INTRODUCTION

The cloud G110−13 (BM Andromedae: $d = 440$ pc) was originally examined by Aveni & Hunter (1969) as part of their survey of small early-type star clusters with $M < 200\ M_\odot$. They concluded that the star-forming episode in this "tear-shaped" cloud, and in others of comparable mass, may have been initiated by a nongravitational mechanism possibly related to a thermal instability, which might also account for its unusually high star-forming efficiency. More recently, Odenwald & Rickard (1987) and Odenwald (1988) found that this cloud has a striking, highly elongated, comet-like shape at far-IR wavelengths (see Fig. 1). This distinctive shape makes it unique among the 14 additional "head-tail" clouds identified in the *IRAS* data at high Galactic latitudes. It has been speculated that these far-IR, head-tail clouds may owe their comet-like shapes to their interaction with the ambient interstellar medium; small clouds moving through a dense medium could lose material by gas stripping, giving them a distinctive, streamlined shape (Odenwald 1988). The elongated Draco Cloud described by Goerigk et al. (1983) and by Odenwald & Rickard (1987) is an example of such an interaction in a low-mass, high Galactic latitude molecular cloud. The presence of active star-forming regions in several of the clouds identified by Odenwald & Rickard (1987), including G110−13, also suggests that at least some clouds may have been compressed by rampressure, thereby triggering star formation in them.

In this article, optical, far-IR, radio continuum, H I, and CO data for G110−13 are combined to determine its detailed physical condition. Also, several scenarios for explaining the morphology and star formation process in G110−13 are explored.

2. OBSERVATIONS

2.1. *Far-Infrared*

The area including G110−13 was studied using co-added images of the far-IR data from each of the four *IRAS* bands obtained from the Infrared Processing and Analysis Center (IPAC). These images include all the brightness data obtained by *IRAS* on the cloud at each wavelength, with a diffuse background component removed from the co-added data at each band. The images are gridded at a scale of 1.0 per pixel at 100 μm, 0.5 at 60 μm and 0.25 at 12 and 25 μm. As a comparison, the *IRAS* beam profiles are 0.75 × 4.5 at 12 and 25 μm, 1.5 × 4.7 at 60 μm, and 3.0 × 5.0 at 100 μm. The resulting far-IR maps are shown in Figure 2.

To obtain information about the dust temperature and opacity distributions, the images at 25, 60, and 100 μm have been converted to T_d and τ using the procedure described by Verter & Rickard (1992). A dust grain emissivity law of $\epsilon(\lambda) = \lambda^{-1.0}$ has been assumed. T_d(60:100) represents the dust temperature derived from the 60 and 100 μm images; T_d(25:60) is the corresponding temperature based on the 25 and 60 μm images. The dust optical depths, τ_{60} and τ_{100}, are based on the 60 and 100 μm images along with T_d(25:60) and T_d(60:100), respectively. The resulting gray-scaled maps of T_d and τ, shown in Figure 3, also included the 60 μm surface brightness contour at a level of 1.8×10^{-8} W m^{-1} sr^{-1}. This contour level will be used throughout the discussion to define the cloud's extent.

A search through the *IRAS* Point Source Catalog (PSC) revealed five unresolved far-IR sources within the boundaries of the cloud. In Table 1, column (1) identifies the *IRAS* point source, columns (2)–(5) present the far-IR flux densities in each of the four bands, and column (6) gives the *IRAS* Structure Correlation (SC) index. This index indicates whether the source is completely unresolved (SC = 'A') or whether the source profile is significantly broader than the detector beam in a particular band (SC = "B" − "M").

2.2. *Radio Continuum*

Radio continuum observations of G110−13 were obtained on 1986 November 29 using the NRAO Very Large Array in the C configuration at 4.89 GHz. The two fields shown in Figure 4*a* were observed with a synthesized beam of 6.6 × 3.7 at P.A. = −81°, where the position angle is measured clockwise from north. Each field was observed for ∼30 minutes in left and right circular polarization with a 50 MHz bandwidth. "CLEANed" radio maps were generated from the data using the AIPS MX routine with natural weighting.

Because of telescope time limitations, all of G110−13 could not be observed. Two fields were selected, one that includes the

[1] BDM, International, Suite 340, 409 Third Street, SW, Washington, DC 20024 (Postal address for S.O.).
[2] Code 4213.8. Center for Advanced Space Sensing, NRL, Washington, DC 20375 (Postal address for J. F.).
[3] NRAO, 520 Edgemont Road, Charlottesville, VA 22903. The National Radio Astronomical Observatory is operated by Associated Universities, Inc. under a cooperative agreement with the National Science Foundation.
[4] Applied Research Corp., Landover, MD 20785. Postal address: Code 4213.S, NRL, Washington, DC 20375.

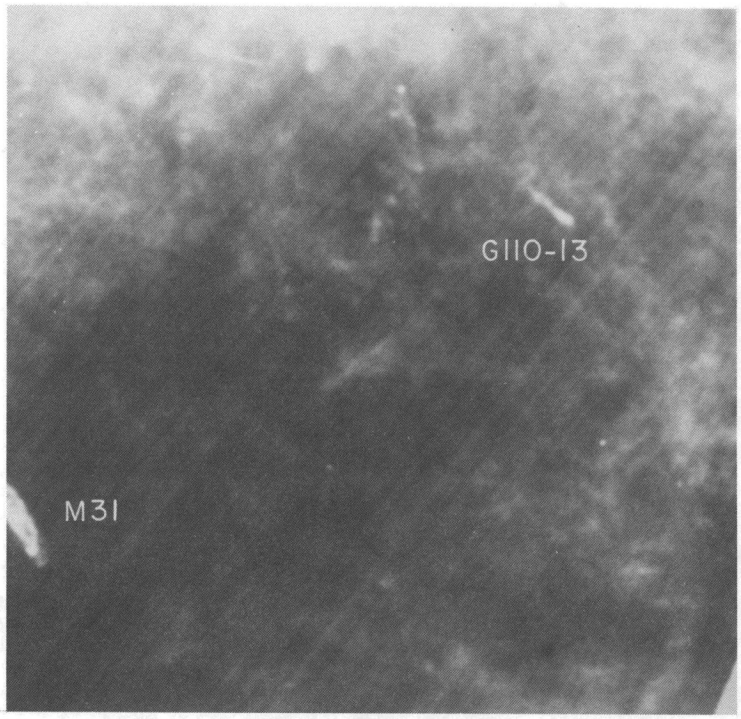

FIG. 1.—HCON-1 Skyflux Plate 027 showing the 100 μm far-IR background in the vicinity of G110−13, which is located in the upper right corner of the image

far-IR peak region, and one that includes the secondary peak near the middle of the extended far-IR emission. Since the primary antenna beam FWHM is $\approx 9'$ at 4.89 GHz, only a small portion of the nebula was observed with good sensitivity. In Figure 4*a* we show the fields observed, and the region in which the rms level achieved was ≈ 0.5 mJy/beam^{-1}, superposed on a Palomar Observatory Sky Survey (POSS) 103a-E photograph. The properties of the detected sources are summarized in Table 2 wherein columns (1)–(3) give the source identification and position, and column (4) gives the measured total flux and associated rms error.

2.3. *21 Centimeter* H I

The H I spectral line data were obtained using the NRAO 43 m telescope at Green Bank, West Virginia, on 1987 October 5–6 as part of a systematic survey (Odenwald & Lockman 1992) of the far-IR clouds identified by Odenwald & Rickard (1987). The telescope beam is 21′ (FWHM) at 1420 MHz. The spectra covered a velocity range of ± 250 km s^{-1} centered at $V_{LSR} = 0$ km s^{-1} with a resolution of 1 km s^{-1}, and were obtained every 10′ in right ascension and declination so that the maps are fully sampled in both directions. The integration time per spectrum was 20 s, yielding an rms noise level per channel of 0.1 K. Representative H I spectra within G110−13 are shown in Figure 5.

Table 3 summarizes the H I and far-IR properties of selected points in the cloud within its Head and Tail components: columns (1) and (2) give the 1950.0 right ascension and declination of the beam position; columns (3) and (4), the total far-IR surface brightness measured at 60 and 100 μm in the HCON-1 Skyflux image without background subtraction; column (5), the integrated H I emission over the full velocity interval; column (6) indicates the ratio of the far-IR emission at 100 μm to the total H I column density in units of 10^{-14} Jy sr^{-1} (atoms cm^{-2})$^{-1}$; column (7) gives the dust temperature, and column (8) is the depth at 100 μm as described above.

TABLE 1

IRAS POINT SOURCES NEAR G110−13

NAME (1)	FAR-IR FLUX DENSITY 12 μm (Jy) (2)	25 μm (Jy) (3)	60 μm (Jy) (4)	100 μm (Jy) (5)	*IRAS* STRUCTURE INDEX (6)
23339+4811.....	<0.33	0.62	<0.74	<3.5	FBB–
23346+4811.....	<0.25	<0.33	1.83	<19.6	–JBH
23350+4815.....	0.58	<0.24	<0.36	<35.3	BG––
23353+4812.....	0.53	0.72	5.46	<36.2	DEEC
23379+4842.....	<0.25	<0.24	<0.36	3.8	––– C

TABLE 2

RADIO SOURCES NEAR G110−13

Name (1)	α(1950) (2)	δ(1950) (3)	S_p (mJy) (4)	Remarks (5)
A	$23^h35^m26^s.3$	48°15′40″.4	7.29 ± 0.34	Unresolved
B.....	23 36 25.3	48 33 15.8	0.88 ± 0.16	Unresolved
C	23 36 29.8	48 33 57.0	4.81 ± 0.45	Extended double 10″.4 separation
D1	23 36 42.7	48 28 12.2	2.30 ± 0.16	Extended, FWHP ~ 7″
D2	23 36 44.5	48 28 33.0	3.66 ± 0.21	Extended, FWHP ~ 8″
E.....	23 36 40.2	48 25 17.3	1.11 ± 0.20	Unresolved: with faint visible star

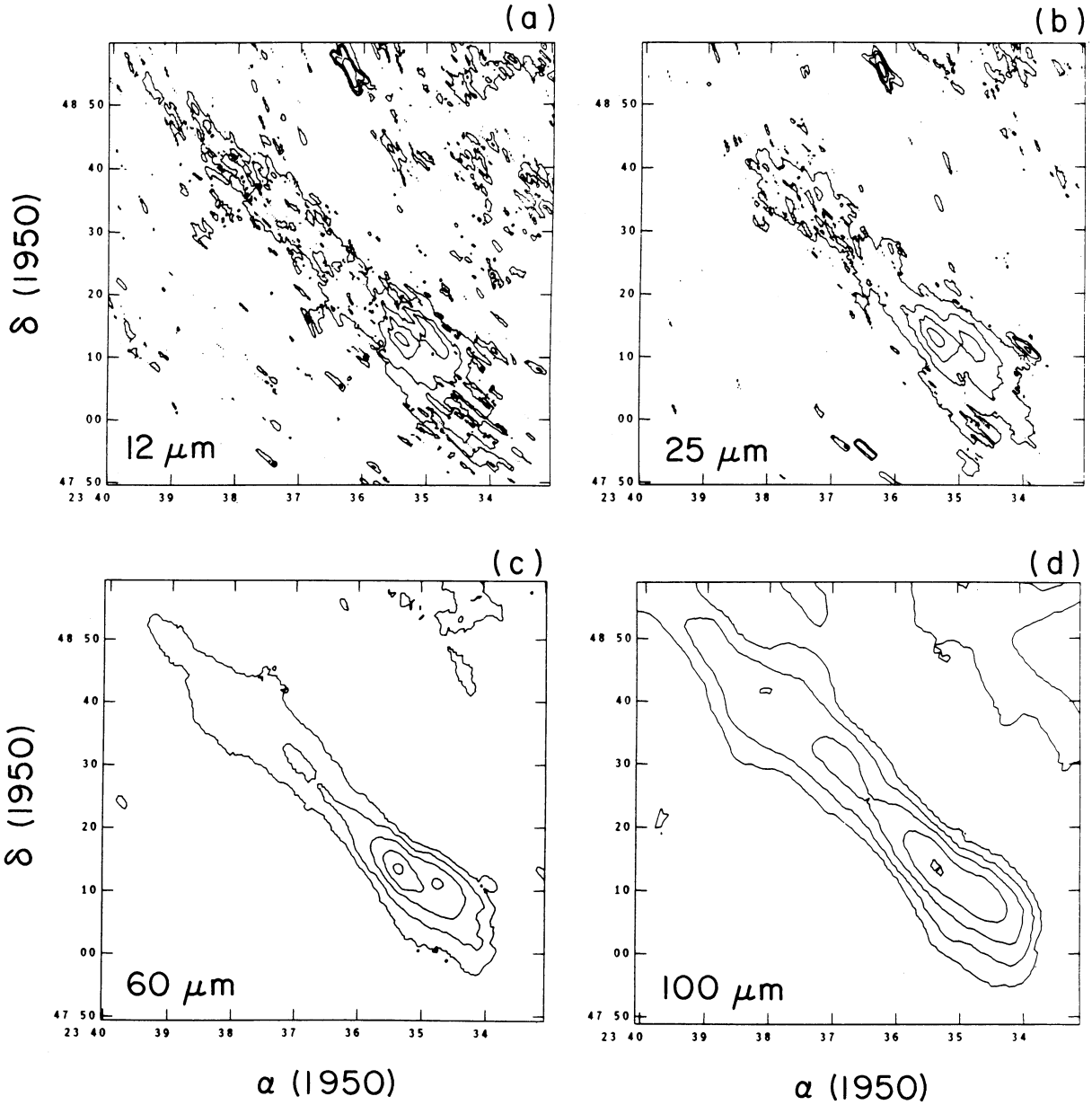

FIG. 2.—Far-IR maps of G110−13. Contours are given in the following multiples of 1.8×10^{-8} W m^{-2} sr^{-1}. (*a*) 12 μm: 2, 4, 8, and 16. (*b*) 25 μm: 1, 2, 4, and 8. (*c*) 60 μm: 1, 2, 4, 8, and 16. (*d*) 100 μm: 1, 2, 4, 8, and 16.

2.4. ^{12}CO ($J = 1$–0)

The ^{12}CO $J = 1$–0 (115.2712 GHz) data were obtained with the NRAO 12 m telescope on Kitt Peak near Tucson, Arizona, on 1989 February 7. The survey was conducted with the 250 and 100 kHz filter banks operated in parallel, centered at $V_{LSR} = 0.0$ km s^{-1} with a resolution of 0.65 and 0.26 km s^{-1} per channel, respectively. The beam size was 55″; the telescope focus and flux calibration were checked at the beginning and at the end of the observing session using the continuum source DR21(OH) as a reference. The data have been corrected for a forward scattering efficiency, $\eta_{fss} \approx 0.75$, and are given in terms of T_R^* which is related to the brightness temperature via $T_B = T_R^*/\eta_S$ where η_S is the source coupling efficiency. Since the cloud size greatly exceeds the ^{12}CO beam size, η_S is of order unity.

G113−13 was mapped by integrating for 1 minute at each of 47 positions within the head of the cloud on a grid with 1′.5 beam spacings. Each measurement was followed by a 1 minute integration at a reference position located at $\alpha = 23^h35^m$ and $\delta = 47°30'$ for which $T_R^* < 0.5$ K. A linear baseline component was then subtracted from each spectrum using the outer 30 channels to establish an off-line reference level. A contour plot of T_R^* has been superimposed on a POSS 103a-O photograph shown in Figure 6, and on the map of τ_{100} in Figure 7. The boundary of the far-IR emission is denoted by the dashed line.

3. RESULTS

3.1. *Far-Infrared*

The remarkable comet-like morphology of G110−13 makes it one of the more unusual, isolated, clouds in the catalog by

Odenwald & Rickard (1987). It is not directly connected to other areas of diffuse far-IR emission in this region of the sky. The cloud has an appreciable aspect ratio (10:1), and its southern end teminates in a bright knot which we call the Head. The cloud has a typical width of 8′ which, for the 440 pc distance estimated by Aveni & Hunter (1969) from spectroscopic parallaxes, corresponds to 1 pc. The component that we identify as the Tail extends ≈1°.4 (10 pc) northeast of the Head before abruptly changing direction northward, becoming twisted into a kink- or looplike feature which is apparent in Figure 1. The Tail is not a uniform filament, but contains three equally spaced clumps with separations of 16′ (2.3 pc). The major axis of the cloud is at a position angle of ≈45°, and is oriented toward a small cluster of late, B-type stars identified as NGC 7801 located 4° northeast of the Head. Unlike the "cirrus" clouds studied by Weiland et al. (1986), there appears to be no excess 12 μm emission from G110−13, based on a smooth extrapolation of the 25–100 μm surface brightness measurements.

The distribution of T_d(60:100) in Figure 3*a* shows that the Tail is virtually isothermal with $\langle T_d \rangle \approx 25$ K. The Head contains two prominent temperature peaks at $\alpha = 23^h35^m.4$, $\delta =$

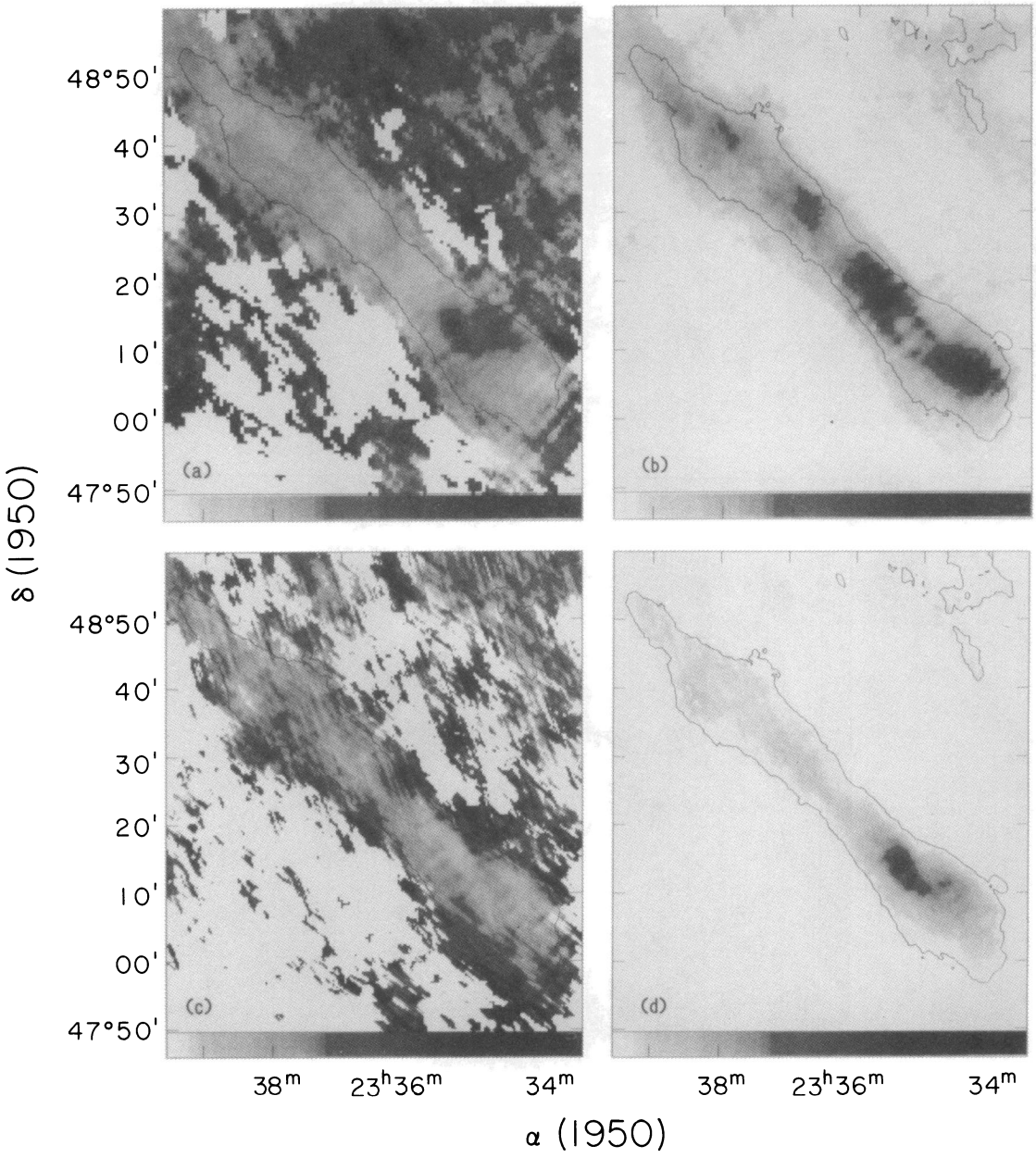

FIG. 3.—Dust temperature and optical depth distribution. (*a*) Dust temperature map showing the distribution of T_d(60:100). The gray-scale wedge covers the range 20 K < T_d < 40 K. Also shown is the lowest 60 μm surface brightness contour to identify the cloud extent. (*b*) The 100 μm optical depth, τ_{100}, based on the 100 μm surface brightness map and T_d(60:100), and tracing the distribution of the cool dust in the cloud. The gray-scale wedge covers the range $0 < \tau_{100} < 2.3 \times 10^{-4}$. (*c*) T_d(25:60) dust temperature distribution. The gray-scaled wedge covers the range 60 < T_d < 120 K. (*d*) The 60 μm optical depth, τ_{60}, tracing the warm dust component, based on the 60 μm surface brightness map and T_d(25:60). The gray-scale wedge covers the range from $0 < \tau_{60} < 2 \times 10^{-6}$.

1992ApJ...397..1740

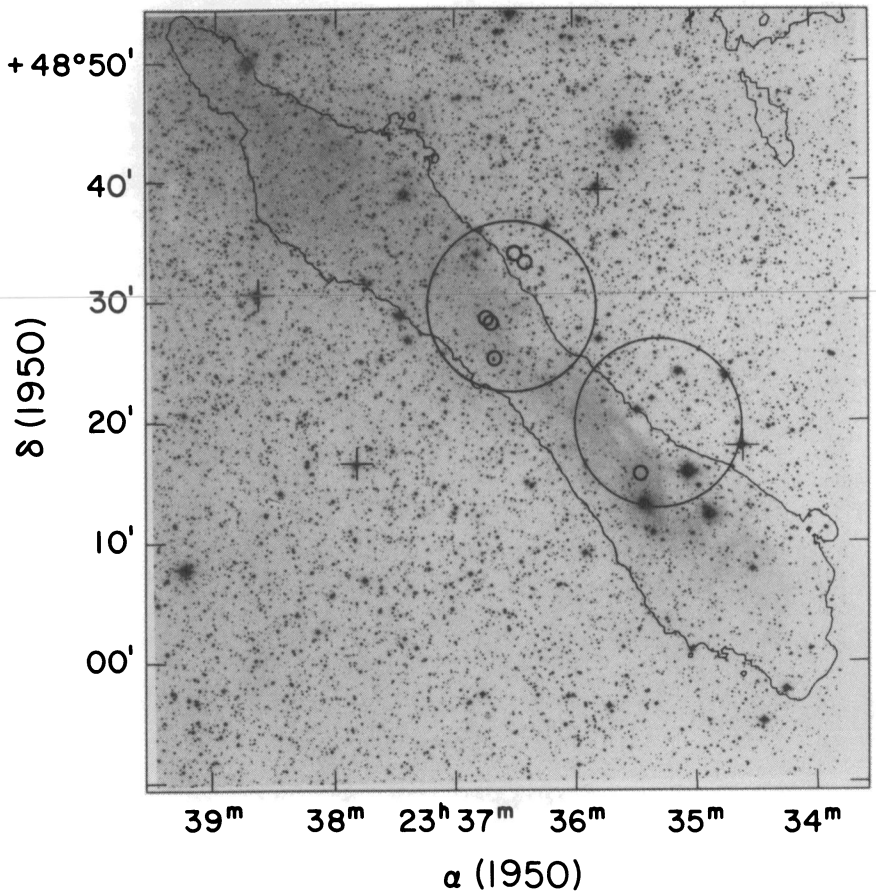

FIG. 4*a*

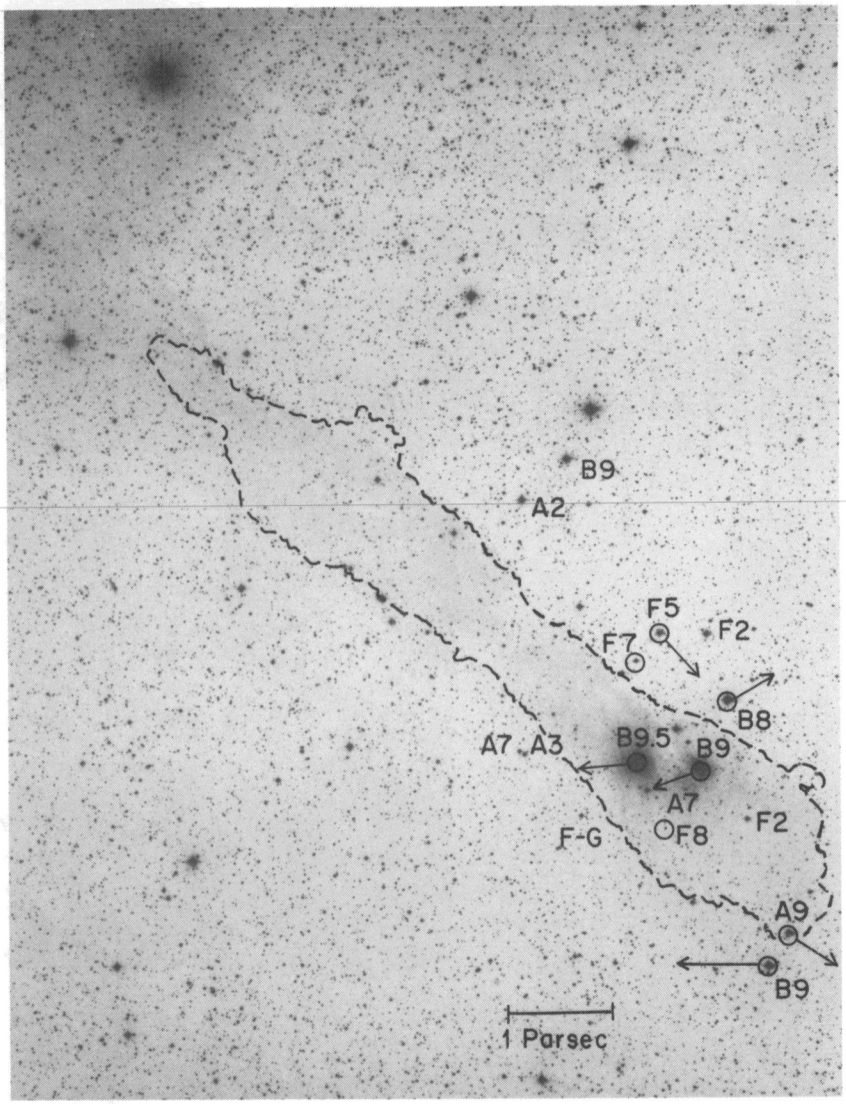

FIG. 4*b*

FIG. 4.—Optical field of G110−13, including the lowest 60 μm surface brightness contour to identify the extent of the cloud. (*a*) POSS 103a-E photograph showing the regions surveyed by VLA, indicated by FWHM of primary beam, and detected radio continuum sources shown by circles. (*b*) POSS 103a-O print showing the spectral types of member stars (*circled*) and uncertain members based on the study by Aveni & Hunter (1969). Also indicated by arrows are the proper motion vectors of the member stars appearing in Table 4.

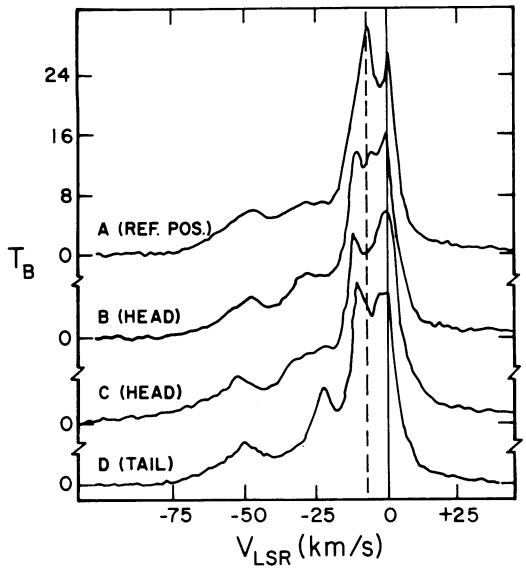

FIG. 5.—H I spectra of G110−13, some of which showing a self-absorption feature near −8 km s^{-1}. Spectra obtained at an off-cloud reference position (A) near $\alpha = 23^h34^m.4$, $\delta = 48°20'$; two positions near the Head region (B, C) at $\alpha = 23^h36^m.4$, $\delta = 48°20'$ and $\alpha = 23^h37^m.4$, $\delta = 48°20'$; and a position near the end of the Tail (D) at $\alpha = 23^h38^m.5$, $\delta = 48°40'$. The vertical, dashed line indicates the velocity of the detected ^{12}CO feature. The solid vertical line indicates $V_{LSR} = 0$ km s^{-1}.

TABLE 3

H I AND FAR-IR EMISSION AT SELECTED POINTS

R.A. (1)	Decl. (2)	S100 (mJy sr^{-1}) (3)	S60 (mJy sr^{-1}) (4)	$W_{H\,I}$ (K km s^{-1}) (5)	R^a (6)	T_d^b (K) (7)	τ^c (8)
$23^h39^m.0$	49°00′	2.1	0.35	93.9	1.23	18.8	110
23 39.5	48 40	1.8	0.39	71.5	1.37	19.8	64
23 38.5	48 40	2.9	1.32	79.9	1.98	23.3	35
23 37.0	48 20	1.9	0.09	35.9	2.89	15.0	692
23 37.5	48 40	2.8	0.77	97.3	1.58	20.8	70
23 36.5	48 20	3.9	1.43	43.6	4.89	22.2	63
23 36.5	48 40	1.9	0.45	115.9	0.93	20.1	61
23 35.5	48 20	4.4	0.89	47.8	5.08	19.5	175
23 35.5	48 40	1.6	0.24	125.7	0.69	18.4	99
23 34.5	48 20	3.8	0.48	23.1	8.98	17.8	306

[a] In units of 10^{-14} Jy sr H^{-1} atoms cm^{-2}.
[b] Based on the 60 and 100 μm data.
[c] Given in multiples of 10^{-6}.

48°13′.4 and $\alpha = 23^h35^m.2$, $\delta = 48°11'.4$ that have $T_d(60:100) =$ 34 and 32 K, respectively. They are adjacent to the partially embedded B9.5 star, BD +47°4220. The two opacity minima shown in Figure 3*b* coincide with the temperature peaks and may be artifacts of the dust temperature that was adopted. Since $T_d(60:100)$ was determined from the ratio of the 60 and 100 μm emission, it will be biased in favor of the warm dust component which contributes to the far-IR surface brightness at 60 μm. On the other hand, the 100 μm emission from which τ_{100} is determined may have a significant contribution from cold dust grains in the cloud. In either case, the result is that the opacity at 100 μm will be underestimated if appreciable quantities of dust are present in the cloud that are much warmer or cooler than ≈20 K.

This problem is inherent to any model in which the emission is approximated by a population of dust grains at a single temperature, rather than a model with dust grains at a variety of temperatures. The distribution of warm dust is shown in Figures 3*c* and 3*d*. Note that the local minima in τ_{100} are mirrored by peaks in τ_{60} contributed by the warm dust grains.

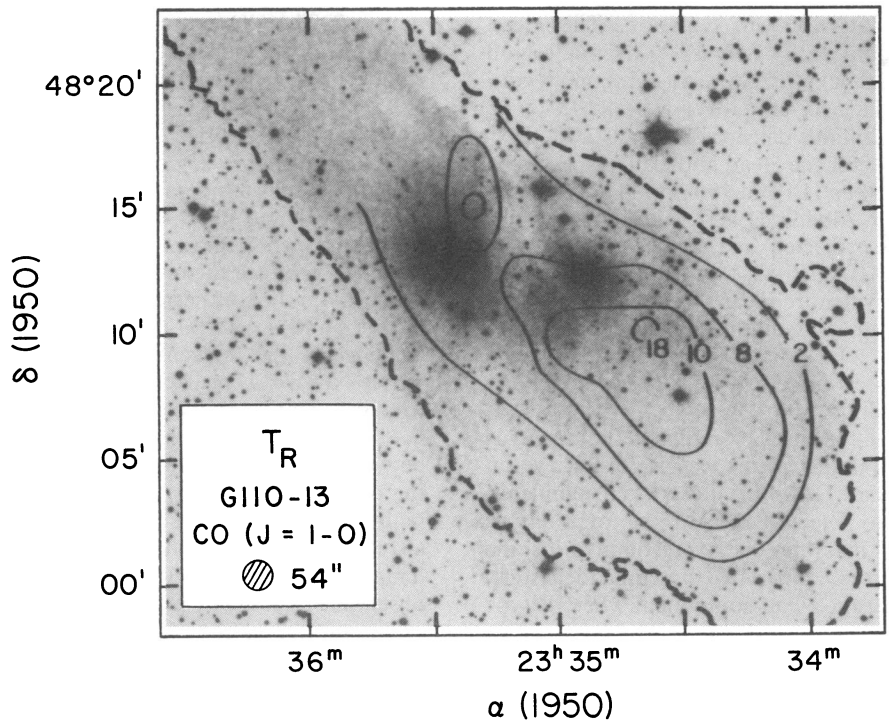

FIG. 6.—The distribution of T_R^* for ^{12}CO (J = 1–0) superposed on POSS 103a-O photograph

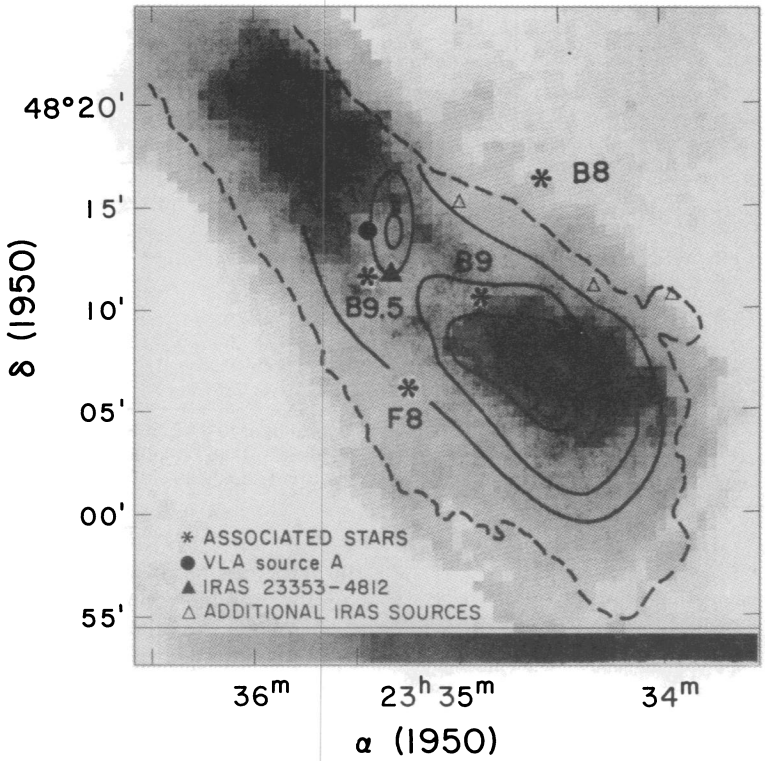

FIG. 7.—^{12}CO ($J = 1$–0) map of G110−13 "Head" region obtained at 55″ resolution and represented as a contour plot in terms of T_R^* at intervals of 2, 8, 10, and 18 K superposed on a gray-scaled dust optical depth map. Also shown are the positions of the associated stars (*asterisk*), the radio source G110−13A (*filled circle*), and IRAS 23353+4812 (*filled triangle*) and the remaining *IRAS* point sources in the field (*open triangles*). The extent of the cloud at 60 μm is indicated by the dashed line. The gray-scale wedge covers the range from $0 < \tau_{100} < 2.6 \times 10^{-4}$.

The dust distribution may in actuality be smoother than the opacity distribution determined from the *IRAS* measurements.

Since the cloud is optically thin in the far-IR, its total mass may be estimated from its 100 μm emission. The Head component has $\langle S(100\ \mu\text{m})\rangle = 28$ mJy sr^{-1} over a region extending 8′ × 20′(1.0 × 3.0 pc), while the Tail component contributes $\langle S(100\ \mu\text{m})\rangle = 5.8$ mJy sr^{-1} over 8′ × 40′(1.0 × 5.5 pc). This implies an H I column density of $N_{\text{H I}} = 2.0 \times 10^{21}$ cm^{-2} and 4.1×10^{20} cm^{-2} for the Head and Tail, respectively, using the relationship between H I and 100 μm flux derived by Boulanger, Baud, & van Albada (1985) for low-extinction cirrus. Integrated over the projected area, the Head has $M_{\text{H}} = 44\ M_\odot$ and the Tail has $M_T = 16\ M_\odot$ for a total cloud mass $M_C = 60\ M_\odot$. This is equivalent to mean gas densities of $n_{\text{H}} = 430$ cm^{-3} and $n_T = 85$ cm^{-3} assuming the components are cylindrical in shape. The cloud's mass determined this way is comparable to the 40 $M_\odot$ estimate by Aveni & Hunter (1969) derived from optical extinction data.

If the gas-to-dust ratio in the cloud is similar to that in cirrus clouds, the total mass estimated in this way is correct even if some of the gas is molecular. However, if there is a significant amount of dust too cold to detect at 100 μm, the total mass is underestimated. The total mass may be overestimated if some of the emission at 100 μm is contributed by embedded stars, which could be the case for the Head component where B-type stars are in evidence.

3.2. *Molecular Gas*

^{12}CO ($J = 1$–0) emission was detected in the Head at $V_{\text{LSR}} = -7.7$ km s^{-1} with ΔV(fwhm) = 1.4 km s^{-1}. The V_{LSR} is consistent with galactic rotation at the location of the nebula (e.g., Brand, Blitz, & Wouterloot, 1988). The relationship between the molecular gas and dust components is shown in Figure 7. The CO emission traced by T_R^* follows the general distribution of the dust in the Head at an optical depth of $\tau_{100} \approx 10^{-4}$. Of particular interest is the isolated CO hot spot at $\alpha = 23^{\text{h}}35^{\text{m}}.3$ and $\delta = 48°15'$ which is in the immediate vicinity of both BD +47°4220, and the northernmost dust temperature peak ($\alpha = 23^{\text{h}}35^{\text{m}}.4$; $\delta = 48°13'.4$) where $T_d(60{:}100) = 34$ K. The dust temperature peak is located midway between the CO peak and BD +47°4220, which suggests that the star is heating some of the dust near the surface of the molecular clump to produce the CO hot spot. A similar geometry would also explain the southernmost dust temperature peak near $\alpha = 23^{\text{h}}35^{\text{m}}.3$ and $\delta = 48°11'.4$ located between BD +47°4220 and the edge of the molecular material in the Head. While one might expect a T_d peak to coincide with a T_{CO} peak, according to a gas heating model by Goldreich & Kwan (1974) if the molecular densities are below 2×10^4 cm^{-3} the coupling between the gas and dust components will be inefficient, and the dust will no longer be effective in maintaining the gas at high temperatures. We should then expect that at low densities, a dust temperature peak will not always coincide with a CO temperature peak. Additional ^{13}CO and other molecular line observations could help to resolve these uncertainties.

The molecular content of the Head may be estimated from ^{12}CO $J = 1$–0 line strength. A lower limit is given by the optically thin value

$$N(\text{H}_2) > 2.5 \times 10^{20} W(\text{CO})\ \text{cm}^{-2}\ . \qquad (1)$$

Since $W(CO) = 16$ K km s^{-1}, the estimated molecular hydrogen column density $N(H_2) \geq 4 \times 10^{21}$ cm^{-2}. The extinction estimate corresponding to this value, $A_V \geq +4^m.3$, is consistent with the maximum extinction inferred by Aveni & Hunter (1969) of $A_V = +2.07$ for the partially embedded, T Tauri–like star BM Andromedae. The total mass in the Head, for a projected surface area of 1.0 × 3.0 pc is then $M(H_2) \geq 85\ M_\odot$, which is only 50% greater than the mass estimated from the 100 μm flux.

3.3. *Atomic Hydrogen*

H I spectra toward G110−13 have a relative minimum at the velocity of the ^{12}CO emission, as shown in Figure 5, suggesting that the H I associated with the nebula is self-absorbed. Figure 8 shows the difference between the H I emission toward the Head and that at a reference position several degrees away. The deep self-absorbed component near −8 km s^{-1} can be traced over much of G110−13 at a brightness temperature 6–10 K lower than at the reference position, corresponding to H I opacities of 0.3−0.4. Opacities of this magnitude have been derived by Knapp (1974) for a number of dust clouds. Self-absorption in H I, however, is difficult to interpret quantitatively (e.g., Dickey & Lockman 1990). The observed self-absorption could be produced if less than 1% of the cloud's mass is in H I at a temperature of 10 K. The extensive self-absorption in this cloud does indicate that cool gas, and hence molecules, is likely to be widespread over G110−13 beyond the area we have been able to map in ^{12}CO.

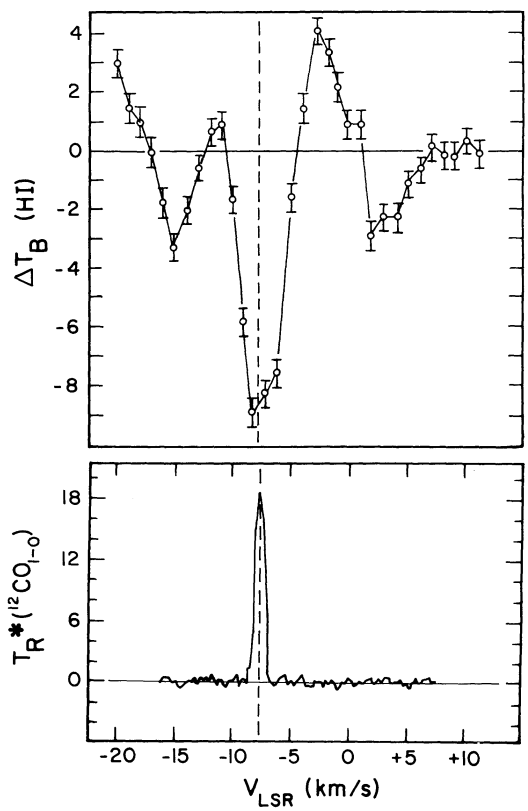

FIG. 8.—Profile of the H I self-absorption feature obtained from the difference between the reference position (A) and the H I spectrum at position (C). Error bars denote the ±0.4 K uncertainty in T_B. Also shown is a representative spectrum of the ^{12}CO ($J = 1$–0) emission from the Head region, at $\alpha = 23^h34^m.6$, $\delta = 48°10'$, demonstrating that the molecular material is at the same velocity as the self-absorbed H I.

A more striking association of H I with G110−13 is shown in Figure 9 where H I emission contours are overlaid on a 100 μm map of the region. The contours show the H I brightness temperature in a 1 km s^{-1} interval and are drawn for only the strongest emission for which $I > 40$ K km s^{-1}, and $-10 < V_{LSR} < +3$. This velocity range includes most of the H I emission in the region.

The brightest H I emission at −9 km s^{-1} and −8 km s^{-1} lies in a ridge with a similar position angle and extent as G110−13, offset ≈15′ to the southeast. This H I cloud is only seen over $-9.5 < V_{LSR} < -6.5$ km s^{-1}. It has a peak $N(H\ I) = 3 \times 10^{20}$ cm^{-2} adjacent to both the Tail and Head. At velocities more positive than −6.5 km s^{-1} the H I emission southeast of G110−13 becomes weak, while there is a bright H I feature northwest of the nebula that has a broad density gradient running parallel to G110−13. Some far-IR features of the Tail component appear to be reflected in the shape of the H I contours, e.g., the kink in the Tail is matched by a 90° change in the gradient of the H I contours at −6 and −5 km s^{-1}.

The association between the −8 km s^{-1} H I, the −6 km s^{-1} H I, and the 100 μm emission is shown clearly in Figure 10 where their intensities are plotted along cuts perpendicular to the nebula through the Head and Tail. Along the cut through the Head, the H I at the two velocities overlaps on the sky and the 100 μm emission is located along the "leading edge" of the −8 km s^{-1} cloud, which is ∼0°.5 wide at this position. At a location on the Tail, the two concentrations of H I are more separated and the 100 μm emission is more clearly connected with the −8 km s^{-1} cloud which is 0°.7 wide there.

Our interpretation of these data, which will be developed in the next section, is that G100−13 is part of the −8 km s^{-1} cloud and was formed by the interaction between that cloud and the H I at −6 km s^{-1}. We suggest that the collision is more advanced at the southern end of the nebula, where much of the H I along the collision front has become molecular and where the 100 μm peak is thus displaced from the H I peak. Along the Tail, where the two H I features are not fully overlapping on the sky, there has been less conversion of H I to H_2 so the infrared emission is weaker and occurs on the main H I peak. The ratio $\langle N_H(100\ \mu m)\rangle / \langle N_H(21\ cm)\rangle$ is ≈20 near the Head and ≈3 along the Tail.

3.4. *Radio and Far-IR Sources*

The six radio continuum sources summarized in Table 2 were detected in the VLA fields which are shown in Figure 4*a*. Since, with the exception of Source E, they are not coincident with local maxima in the dust temperature, or 100 μm surface brightness peaks, it is unlikely that most of these sources are related to G110−13. Source E coincides with a faint star with $m_r \approx +18^m$ which has no associated nebulosity. Insufficient data exist at the present time to determine whether it is a T Tauri star, possibly associated with the cloud, or an unrelated background or foreground star. Sources C and D are double-lobed and are probably extragalactic while source B is uncertain and may, or may not be extragalactic. A 6 cm survey by Bennett et al. (1983), covering a total area of 2100 square arcminutes with the VLA, detected 16 extragalactic radio sources with $0.8 < S(mJy) < 6.0$, including one double-lobed radio galaxy. Scaling their detection rate to the 200 square arcmin-

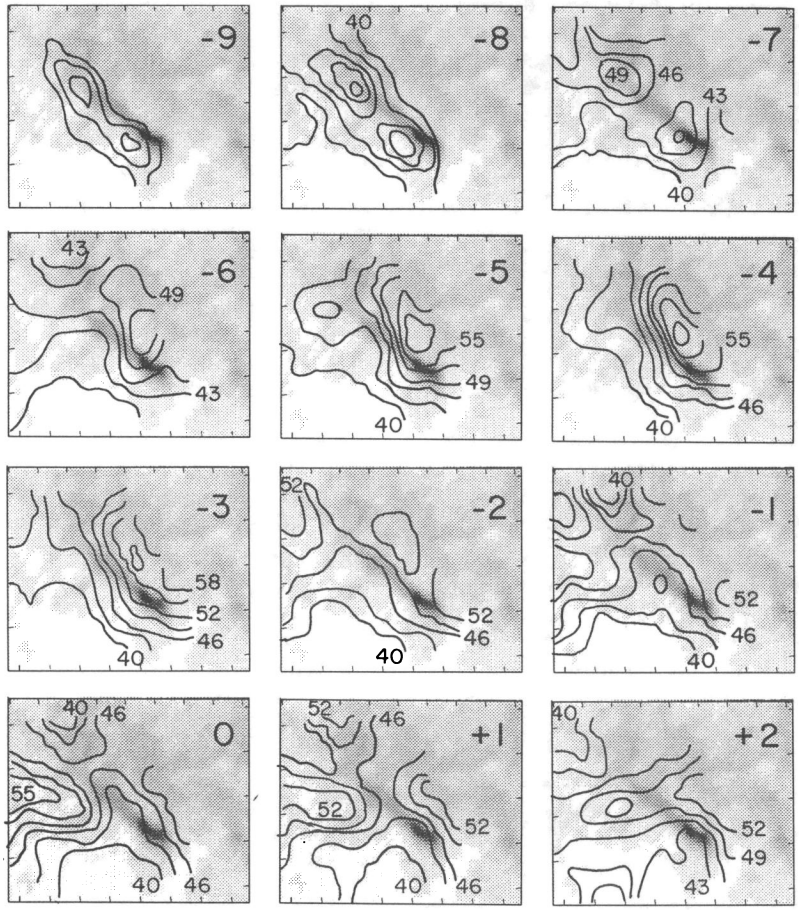

FIG. 9.—H I channel maps. The declination axis increments are in 30′ intervals while the right ascension axis increments are in intervals of 5^m. The contour intervals begin at 40 K km s^{-1} and are presented at increments of 3 K km s^{-1}. The gray-scale plot is that of the 100 μm data from the *IRAS* HCON-1 Skyflux data.

utes covered in this survey, we expect roughly two background extragalactic radio sources, which is consistent with our findings.

Source A is situated near a prominent far-IR source in G110−13, IRAS 23353+4812, located at $\alpha = 23^h35^m20^s.4$, $\delta = 48°12'53''$. It is within the cloud boundaries and is approximately coincident with both the secondary CO hot spot and the northernmost dust temperature peak shown in Figure 7. This positional coincidence with known tracers of star-forming activity strengthens the argument that Source A is not extragalactic and may be associated with G110−13 itself. This far-IR source has an increasing continuum toward longer wavelengths; a characteristic commonly taken to be an indicator for young stellar objects according to Shu, Adams, & Lizano (1987). The location of Source A in such proximity ($\approx 1'.8$) to IRAS 23353+4812 and a CO peak ($\approx 1'$) in an active star-forming cloud raises the possibility that it may be an embedded young star. The position discrepancies between Source A and these features, however, appear to be significant relative to the anticipated position uncertainties in the CO and far-IR data of $\pm 15''$. The radio emission from Source A may be due to the ionized wind associated with a young stellar object (YSO) located near, or embedded within, the molecular cloud. According to Panagia & Felli (1975), the mass loss associated with a star detected as a radio source is given by

$$dM/dt = 4 \times 10^{-6} S^{0.75} \nu^{0.45} d^{1.5} V(1000)\ M_\odot\ \mathrm{yr}^{-1}\ .$$

If we take $V = 100$ km s^{-1}, $S = 7.3$ mJy, $d = 0.44$ kpc, and $\nu = 5$ GHz then $dM/dt = 5.2 \times 10^{-7}\ M_\odot\ \mathrm{yr}^{-1}$ which is not an unusual mass-loss rate for YSOs.

The far-IR luminosity of IRAS 23353+4812 may be estimated from the measured *IRAS* flux densities in each band (Casoli et al. 1987) using the relation

$$F = 2.2S(12\ \mu\mathrm{m}) + 0.87S(25\ \mu\mathrm{m}) + 0.45S(60\ \mu\mathrm{m}) + 0.18S(100\ \mu\mathrm{m})\ ,$$

where the total flux, F, is given in units of 10^{-13} W m^{-2} and the in-bank flux densities, S, are given in terms of janskys. In terms of the *IRAS* flux densities in Table 1, $F < 1.1 \times 10^{-12}$ W m^{-2} if the upper limit to $S(100\ \mu\mathrm{m})$ is used, and $F > 4.2 \times 10^{-13}$ if only the 12–60 μm measurements are used. At a distance of 440 pc, and assuming isotropic emission, the far-IR luminosity is $2 < L_{\mathrm{fir}}/L_\odot < 6$. If IRAS 23353+4812 is not internally heated but represents the emission from dust located near the edge of the molecular cloud peak heated by BD +47°4220, less than 17% of this star's estimated bolometric luminosity ($\approx 35\ L_\odot$) would be required to heat the dust and thereby account for the $L_{\mathrm{fir}} \approx 6\ L_\odot$ detected. The apparent lack of a detectable radio source coinciding with the externally heated far-IR peak would, in this circumstance, not be unexpected. One final possibility is that Source A is a background galaxy. Clearly, additional radio continuum measure-

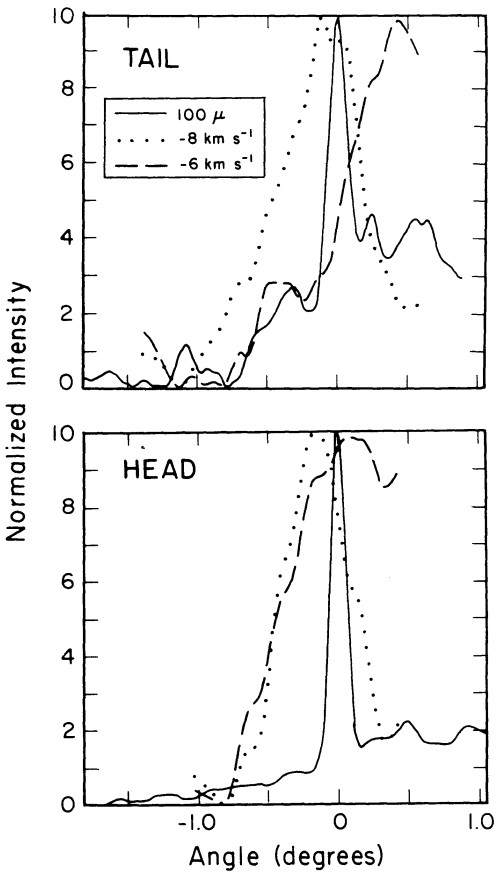

FIG. 10.—H I and 100 μm slices through the Head and Tail regions of G100−13. The intensities along each one-dimensional slice have been normalized to 10.0 at the location of peak emission. The horizontal scale indicates the angular offset of the H I emission relative to the far-IR emission in degrees of arcseconds.

ments will be needed to determine whether the source has a thermal or a nonthermal spectrum and to distinguish between these two possibilities.

The remaining far-IR sources listed in Table 1 and shown in Figures 4*a* and 7 are unremarkable and are detected in only one of the four *IRAS* bands. One of them, 23350+4815, was detected only at 12 μm and coincides with the K0 star SAO 53199. Since the point source extraction algorithm is known to confuse sharp gradients in the 25–100 μm surface brightness with point sources, no further consideration will be given to these sources at this time.

3.5. *Stellar Component*

Spectroscopic observations by Aveni & Hunter (1969) of 24 stars adjacent to G110−13 previously revealed that at least eight were not associated with the cloud on the basis of their spectroscopic parallax. Of the remaining 16 stars, only the eight shown in the POSS 103a-O photograph in Figure 4*b* were identified as members, either in terms of a common spectroscopic parallax, or a clear physical association with the cloud nebulosity. Two B-type stars, BD +47°4220, are clearly embedded within the cloud and have spectroscopic parallaxes implying a mean distance of 440 ± 100 pc. Moreover, the locations of the member stars on a color-magnitude diagram indicate that stars later than approximately A0 have not yet contracted onto the main sequence. The age of the association was, therefore, estimated by Aveni & Hunter (1969) as $\approx 4 \times 10^6$ yr. The stellar mass contribution, including ≈ 10 $M_\odot$ in the uncertain stellar members, was estimated as $M^* \approx 30\ M_\odot$. When compared with the cloud's mass estimate of $M_c \approx 60\ M_\odot$ derived from the far-IR observations, the total initial cloud mass was probably in excess of 90 $M_\odot$, so that the estimated star formation efficiency is ≈30%. The total stellar mass is an estimate since not all of the stars associated with the cloud may have been identified, while the total cloud mass is also a lower limit since appreciable quantities of cold dust grains may be present but not detectable in the *IRAS* bands.

Odenwald (1988) estimated a total far-IR luminosity of the cloud which corresponds to $L_{\rm fir} = 34\ L_\odot$ at the currently adopted distance of 440 pc. Tabulations of OB star ionizing continuum by Thompson (1984) suggest that the bolometric luminosities for B9 and a B9.5 V stars are $L^* = 55$ and $L^* = 35$, respectively, so that the two embedded stars, BD +47°4220 and 4214, by themselves contribute $L^* \approx 90\ L_\odot$. The detected far-IR luminosity of G110+13 is, therefore, only 25% of the total stellar emission. Since $L_{\rm fir}$ may also include a contribution from the local interstellar radiation field or other embedded low-mass stars, we deduce that more than 75% of the stellar continuum radiation escapes from the star-forming region in G110+13 without being absorbed by the dust grains in the cloud. Comparing the POSS 103a-O and 103a-E photographs we see that the gas and dust near BD +47°4214 and BD +47°4220 show a marked excess in the 103a-O "blue" photograph, which indicates reflection nebulosity and probably significant leakage of stellar UV photons out of the cloud.

Velocity measurements based on spectral line studies are only capable of determining the component of a cloud's space velocity along the line of sight. Since in subsequent discussions it is desirable to know the total space velocity of this cloud, some estimate is needed for the remaining transverse velocity component, V_T. We may estimate V_T by assuming that the stars share the same velocity as the cloud.

Using the AGK 3 star catalog, proper motions have been obtained for some of the brighter stars associated with the cloud. Table 4 includes the BD and SAO designations for comparison with the study by Aveni & Hunter (1969). Column (3) gives the spectral type; column (4), the visual magnitude; column 5 the quantity $A_v = 3\ E(B-V)$; columns (6) and (7) give the proper motion components in right ascension and declination in milli-arcseconds per year (mas yr^{-1}). The magnitude of the resultant proper motion vector, Π, appears in column (8), along with the corresponding velocity in column (9) determined from Π (arcsecs yr^{-1}) = $4.7 \times 10^{-4} V_T$ km s^{-1}. The directions of the proper motion vectors are shown in Figure 4*b*, and yield a total proper motion for the stellar ensemble of $\langle \Pi \rangle = 6.7 \pm 4.4$ mas yr^{-1} at a position angle of P.A. = 135°, with a stellar velocity dispersion $\sigma^* = 18 \pm 4.4$ mas yr^{-1}. Correcting this for the mean projected solar motion yields $\langle \Pi \rangle_c = 14.5 \pm 4.4$ mas yr^{-1} at P.A. = 110°, so that the magnitude of the transverse velocity of the stellar association is $V_T = 31 \pm 9$ km s^{-1}. When combined with the radial velocity component for the ^{12}CO the total space velocity with respect to the local standard of rest can be no greater than $V = 32 \pm 9$ km s^{-1}. An additional correction can be made using the standard Galactic rotation model to compute the cloud's motion relative to its own local ISM from which one obtains $V_{\rm cloud} = 38 \pm 9$ km s^{-1}.

TABLE 4

SUMMARY OF STELLAR DATA

Star BD (1)	Name SAO (2)	Spectral Type (3)	m_v (4)	A_v (5)	Proper Motion[a] $\Delta\alpha$ (mas yr^{-1}) (6)	$\Delta\delta$ (mas yr^{-1}) (7)	π (mas yr^{-1}) (8)	V_T (km s^{-1}) (9)
+47°4217	53205	F5 IV	+9.47	0.46	−9.4	−14.2	17	36
+47°4211	53190	B8 Vp	+8.65	0.09	−9.4	5.8	11	23
+47°4206	53184	A9 III	+9.30	0.12	−8.4	−6.2	10	22
+47°4209	53188	B9 V	+8.94	0.54	31.6	0.8	32	67
+47°4214	53194	B9 V	+8.55	0.18	14.6	−4.2	15	32
+47°4219	...	F7 IV–V	−10.79	0.00	...	...	...	...
+47°4220	53209	B9.5 V	+9.50	0.60	9.6	−10.2	14	30
BM And	...	F8e	12–14	2.07	...	...	...	...

[a] Corrected for a systematic error of $\Delta\alpha = +0.4$ mas yr^{-1} and $\Delta\delta = -1.8$ mas yr^{-1} (Tom Corbin, private communication). The residual random error is ± 8 mas yr^{-1}.

4. DISCUSSION

4.1. *What is G110−13?*

Thus far, we have been able to deduce that G110−13 is an isolated, low-mass cloud with $M_C = 60\ M_\odot$, located 100 pc below the Galactic plane, which is producing stars with an efficiency $\eta = M^*/(M^* + M_C) \approx 30\%$. The narrowness of its ^{12}CO line emission suggests no significant levels of internal turbulence beyond what is often detected in molecular clouds elsewhere in the Galaxy. From the transverse proper motions of the stars associated with the cloud, and the velocity of the molecular emission, the total space velocity of the cloud is probably no more than $V_c \approx 38 \pm 9$ km s^{-1}. In this section we examine possible formation mechanisms for this object and conclude that it is most likely the interface between two colliding clouds.

4.2. *Why Does G110−13 Have a Comet-like Shape?*

The shape of G110−13 may serve as an indicator of the mechanism behind the dynamics of this cloud. A variety of scenarios have been proposed over the years to account for similar morphologies in other astrophysical systems.

4.2.1. *Ionization Fronts and Supernova Impacts*

Head-tail or comet-like shapes in young star-forming regions have been predicted in the "champagne" outflow models by York, Tenorio-Tagle, & Bodenheimer (1984). If a star is born near the edge of a molecular cloud, its expanding ionization front will eventually break out from the cloud surface to form a head-tail radio source. The head component represents H II that is partially confined within the molecular cloud, and the tail traces ionized gas that is flowing from the vicinity of the embedded star into the surrounding low-density ambient medium. Such an interpretation has been offered by Garay, Rodriguez, & van Gorkum (1986) for G34.3+0.2. As another example, the Gum Nebula comet-like clouds studied by Reipurth (1983) appear to be caused by molecular material located in the shadow zones of dense globules being ionized and evaporated by the incident UV radiation from the O4 Ia star Zeta Puppis and associated OB stars located 50–100 pc from the clouds.

Comet-like globules have also been observed near the Cas A supernova remnant by Braun, Gull, & Perels (1987) presumably formed as a result of an impact between the expanding supernova shell and local molecular clouds; They look similar to the cloud shapes produced in numerical calculations by Sofue (1978).

G110−13 does not appear to fit the minimum requirements of such scenarios. It does not contain an embedded O-type star, nor are there any O-type stars within 200 pc of the cloud that could be significant in producing ionization fronts. Moreover, we find no evidence for nearby supernova shells in the Heiles (1984) survey that might have impacted this cloud to produce its shape as in the case for the Cas A globules.

4.2.2. *Ram Pressure*

The mechanism of ram pressure sweeping was originally invoked by De Young & Axford (1967) to account for the parabolic shapes of the lobes of extragalactic radio sources and certain peculiar galaxies such as NGC 3312 (Gallager 1978). On the interstellar scale, studies of the H I fine structure in Galactic high-velocity clouds (HVCs) by Giovanelli & Haynes (1977) have found that some HVC complexes can be resolved into individual cloudlets that often show asymmetric head-tail morphologies. Velocity gradients within these clouds may be evidence for mass loss.

An additional example of the interaction between a rapidly moving cloud and its ambient medium may be found in the Draco Cloud. *IRAS* images described by Odenwald & Rickard (1987) reveal intricate filamentary plumes associated with the main cloud whose properties are consistent with a hydrodynamical origin involving gas stripping. Similar interpretations have been offered by Mebold et al. (1985) and Goerigk et al. (1983). Numerical studies by Hausman (1981), Tenorio-Tagle (1981), and Tenorio-Tagle and Paulos (1987) have shown that many complex morphologies may be obtained when clouds impact the dense interstellar medium in the Galactic plane. Filaments and comet-like shapes are among the common end results of low-velocity impacts.

If the ram pressure scenario is at all applicable to G110−13, it should be possible to obtain a rough estimate of the resulting pressure. The ram pressure experienced by a cloud moving with velocity, V, through a gas with a density ρ is simply $P_{\rm ram} = 1/2\rho V^2$, or $P_{\rm ram}/k = 58n(\rm cm^{-3})V(\rm km\ s^{-1})^2$. Thus, 100 pc from the Galactic plane where the mean density is a few tenths cm^{-3} (Dickey & Lockman 1990) and the thermal pressure is $P/k \approx 4000$ cm^{-3} K (Kulkarni & Heiles 1987), a cloud need only have a peculiar velocity of ≈ 20 km s^{-1} to experience ram pressures comparable to, or greater than, the ambient ISM pressure. Since we have estimated in § 3.5 that the total

space velocity of G110−13 is probably no more than 38 ± 9 km s^{-1}, ram pressure leading to modest over pressures in the Head are indeed possible in this cloud.

Although ram pressure appears to be a possible candidate and was initially proposed by Odenwald (1988) to explain the shape and enhanced star-formation rate in G110−13, there are at least two difficulties with this interpretation that have little or no explanation as yet.

The first of these difficulties is that the stars are not all moving in the same direction as the cloud. The position angles for the two embedded B-type stars are nearly perpendicular to the cloud's NE–SW orientation which is assumed to identify its trajectory through the interstellar medium. The velocity dispersion of the stars is $\sigma = 38$ km s^{-1}, and it is unclear how such large peculiar velocities can arise from ram pressure in a cloud of such a low mass. One possibility may be that the cloud is spawning a population of "runaway stars" which, as described by Leonard & Duncan (1990), are known to have very large peculiar velocities. We note, however, that for cloud-cloud collisions, large stellar peculiar motions may be consistent with the complex velocity fields generated in this manner.

The second difficulty is that the H I and CO data do not show more convincing evidence of a dynamical interaction between the cloud and the ambient interstellar medium. Unless the interaction is so weak as to not stir up the gas in the cloud, one would expect to find either a large peculiar velocity for the gas component in the cloud, or that the H I and CO lines are broadened to turbulence as a consequence of the interaction. Neither of these appears to be the case for G110−13.

4.2.3. *Gravitational and MDH Instabilities*

Recent surveys of low-mass molecular clouds by Magnani, Blitz, & Mundy (1985), Dame et al. (1985), and Keto & Myers (1986), reveal that they can be classified according to whether they are gravitationally bound or not by comparing their internal velocity dispersion with the virial velocity corresponding to the detected mass in each cloud. It is generally found that for the high-latitude clouds, their internal velocities are often an order of magnitude greater than can be gravitationally bound by the gas mass and cloud size deduced from the CO measurements (Myers 1987; Magnani, Blitz, & Mundy 1985). Nevertheless, star formation is occurring even in some of these gravitationally unbound, low-mass clouds such as MBM 20.

For gravitationally bound clouds, the virial line width is given by $\Delta V(\text{fwhm}) = (8 \ln 2GM/5R)^{1/2}$, so that for G110−13, $R = 0.5$ pc and $M_c = 60\ M_\odot$, and one then obtains $\Delta V(\text{fwhm}) = 0.7$ km s^{-1}. The measured ^{12}CO line width is $\Delta V(\text{fwhm}) = 1.4$ km s^{-1} which indicates that the material currently residing in the cloud may not be gravitationally bound. The total mass required for G110−13 to be bound is $M_{\text{viral}} \approx 200\ M_\odot$ which substantially exceeds the current mass residing in the cloud, as well as the total mass including the estimated stellar contribution $M_C = M^* + M_c = 80$–$90\ M_\odot$. We conclude from this that G110−13 is not a gravitationally bound cloud undergoing collapse to form stars; a finding that would seem to contradict the observation that stars are, indeed, forming within the cloud.

Magnetohydrodynamic systems are known to be subject to a variety of instabilities, particularly of the Rayleigh-Taylor type, which have inportant astrophysical consequences. As we noted in § 3.1, the Tail region contains three clumps with a spacing of ≈2.3 pc; a geometry suggestive of a Rayleigh-Taylor instability with the corresponding wavelength. In order for a magnetic field to be effective in controlling the dynamics of the gas and dust in G110−13, the field strength must at least be comparable to the equipartition value given by $P_{\text{int}} = B^2/8\pi$. For the Tail region, we estimated from the far-IR emission that $n_g \approx 85$ cm^{-3}, and for a gas temperature of $T_g \leq T_d = 25$ K, one obtains an internal gas pressure of $P_{\text{int}} \leq 3.6 \times 10^{13}$ dyne cm^{-3}. The corresponding upper limit to the equipartition field strength is then $B_{\text{eq}} \leq 3\ \mu$G, which is similar to the general Galactic field strength. Evidently, the properties of the cloud are in the range for which an MHD instability could be effective with only a modest internal magnetic field.

4.2.4. *Cloud Collision Interfaces*

The possibility that cloud collisions within the Galactic halo may be responsible for forming the early-type stars found there (Trimble 1988) was originally raised by Dyson & Hartquist (1983). According to hydrodynamical modeling by Keto & Lattanzio (1989) collisions between high-latitude clouds can result in the compression and collapse of low-mass interstellar clouds, resulting in conditions suitable for star formation.

The collisions frequently result in the creation of elongated, high-density regions at the collision interface, with major axis oriented perpendicular to the velocity vectors of the colliding clouds. Broad ^{12}CO line wings also result with predicted dispersions of ±8 km s^{-1} relative to the mean cloud V_{LSR}. For low-mass clouds, the effect of the external pressure due to the ambient medium is predicted to be critical in maintaining the long-term integrity of the resulting compressed gas, which is generally found from the numerical simulations to be gravitationally unbound following the collision.

G110−13 appears to fit this scenario well. The relative location of the −8 km s^{-1} cloud, the −6 km s^{-1} cloud and the molecular material sandwiched between them suggests that G110−13 is a region in which the gas in the −8 km s^{-1} cloud has been compressed during the collision. The ^{12}CO line width measurements described in § 4.2.3 imply that G110−13 is gravitationally unbound by factor that is between two and four in mass. Moreover, the clumps identified in the Tail component from the far-IR data have an appearance that is not inconsistent with a MHD instability within this intercloud compression zone.

The radial velocity difference between the two H I clouds is only a few km s^{-1} so their main motion must be across the line of sight. Since the −8 km s^{-1} cloud shares the shape of the IR image while the −6 km s^{-1} cloud is more broadly distributed, we associate the IR image with compressed and swept-up gas at the leading edge of the −8 km s^{-1} cloud, which must be moving approximately to the northwest toward the Galactic plane. In this view, the comet-like shape of G110−13 is somewhat misleading, for it reflects the fact that the −8 km s^{-1} cloud is encountering the other gas at an oblique angle with compression greatest at the Head and less so moving up the tail.

The total mass near the head derived from the 100 μm and 21 cm emission is an order of magnitude larger than that near the Tail, so that the collision did not simply rearrange gas within the −8 km s^{-1} cloud. Most likely a lot of gas was swept up during the interaction.

5. CONCLUSIONS

We have studied the far-IR, H I and CO emission from G110−13 and have attempted to account for its shape by considering a variety of mechanisms likely to be important.

Scenarios involving "champagne" outflows, or interactions with supernova remnants and ionization fronts, seem unable to account for the structure and local environment of the cloud since the prerequisite O-type stars, ionization fronts, or SNRs are not present. Gravitational instabilities seem to be quantitatively unimportant in explaining the global, comet-like shape of this cloud, and star-formation episode now occurring within it. The cloud appears to contain less than one-fourth the mass needed to gravitationally bind it or provide for its gravitational collapse.

If the shape of G110−13 were generated by ram pressure, the cloud's interaction with its local ISM should have been sufficiently energetic to strip material from the cloud's Head to form the trailing tail, while not energetic enough to result in the collisional ionization of the gas or the production of a turbulent gas interface. Estimates for the cloud's total space velocity based on the proper motions of the associated stars yield an inconclusive result, consistent with either no motion relative to its local ISM or a speed that may be considered, at best, moderate, and typical of the random motion of molecular clouds in the Galactic plane.

The most consistent interpretation of the data appears to be that G110−13 is the result of a collision between two interstellar H I clouds whose compression zone defines the elongated far-IR and ^{12}CO emission detected in G110−13. Although G110−13 appears to be gravitationally unbound, nevertheless, stars are forming within it at a prodigious rate compared to more massive molecular clouds. This star formation efficiency may be a direct by-product of the increased external pressure exerted on the cloud during the collision.

Additional ^{13}CO observations would be helpful in establishing the true mass of this cloud, whether the cloud is actually gravitationally unstable and whether cool high-velocity gas is present as predicted by the cloud collision scenario. Since magnetic fields may be a viable alternative for explaining the cloud's shape, optical polarization and H I Zeeman measurements of the low optical depth Tail material should be able to determine whether G110−13 possesses a magnetic field with a suitable strength and topology to be dynamically important.

We would like to thank the NRAO staff at Green Bank and Kitt Peak for their assistance in obtaining the H I and CO data. We are also grateful to Lee J Rickard, John Meekins and Paul Ho for their invaluable suggestions for improving the clarity of the discussions. We are also grateful to Frances Verter and Lee J. Rickard for allowing us to use their *IRAS* data analysis algorithms in advance of publication.

This research was conducted at the Naval Research Laboratory, Naval Center for Advanced Space Sensing. It was supported under NASA's *IRAS* Data analysis Program funded through the Jet Propulsion Laboratory, and by the Office of Naval Research under contract (41-2568-0-0).

REFERENCES

Aveni, A. F., & Hunter, J. H., Jr. 1969, AJ, 74, 1021
Bennett, C. L., Lawrence, C. R., Garcia-Barreto, J. A., Hewitt, J. N., & Burke, B. F. 1983, Nature, 301, 686
Boulanger, F., Baund, B., & van Albada, G. D. 1985, A&A, 144, L9
Brand, J., Blitz, L., & Wouterloot, J. 1988, in The Outer Galaxy, ed. L. Blitz & F. J. Lockman, Lecture Notes in Physics (Heidelberg: Springer), No. 306, 40
Braun, R., Gull, S. F., & Perles, R. A. 1987, Nature, 327, 395
Casoli, F., Dupraz, C., Gerin, M., Combes, F., & Boulanger, F. 1987, A&A, 169, 281
Dame, T., Elmegreen, B., Cohen, R., & Thaddeus, P. 1986, ApJ, 305, 892
De Young, D. S., & Axford, W. I. 1967, Nature, 216, 129
Dickey, J. M., & Lockman, F. J. 1990, ARA&A, 28, 215
Dyson, J. E., & Hartquist, T. W. 1983, MNRAS, 203, 1233
Gallagher, J. S. 1978, ApJ, 223, 386
Garay, G., Rodriguez, L. F., & van Gorkum, J. H. 1986, ApJ, 309, 553
Goerigk, W., Mebold, U., Reif, K., Kalberla, P. M. W., & Velden, L. 1983, A&A, 120, 63
Giovanelli, R., & Haynes, M. P. 1977, A&A, 54, 909
Goldreich, P., & Kwan, J. 1974, ApJ, 189, 441
Hausman, M. A. 1981, ApJ, 245, 72
Heiles, C. 1984, ApJS, 55, 585
IRAS Point Source Catalog. 1985, Joint *IRAS* Science Working Group (Washington, DC: US GPO)
Keto, E., & Lattanzio, J. C. 1989, ApJ, 346, 184
Keto, E., & Myers, P. 1986, ApJ, 304, 466
Knapp, G. R. 1974, AJ, 79, 527
Kulkarni, S. R., & Heiles, C. 1987, in "Interstellar Processes," ed. D. J. Hollenbach & H. A. Thronson, Jr. (Dordrecht: Reidel), 87
Leonard, P. J. T., & Duncan, M. J. 1990, AJ, 99, 608
Magnani, L., Blitz, L., & Mundy, L. 1985, ApJ, 295, 402
Mebold, U., Cernicharo, J., Velden, L., Reif, K., Crezelius, C., & Goerigk, W. 1985, A&A, 151, 427
Myers, P. 1987, in Interstellar Processes, ed. D. J. Hollenbach & H. A. Thronson (Dordrecht: Reidel), 71
Odenwald, S. F. 1988, ApJ, 325, 320
Odenwald, S. F., & Lockman, F. J. 1988, BAAS, 20, No. 4, 957
Odenwald, S. F., & Rickard, L. J 1987, ApJ, 318, 702
Panagia, N., & Felli, M. 1975, A&A, 39, 1
Reipurth, B. 1983, A&A, 117, 183
Shu, F., Adams, F. C., & Lizano, S. 1987, ARAA, 25, 23
Sofue, Y. 1978, A&A, 67, 409
Tenorio-Tagle, G. 1981, A&A, 94, 338
Tenorio-Tagle, G., & Paulous, J. 1987, A&A, 186, 287
Thompson, R. I. 1984, ApJ, 283, 165
Trimble, V. 1988, Nature, 336, 111
Verter, F., & Rickard, L. J. 1992, in preparation
Weiland, J. L., Blitz, L., Dwek, E., Hauser, M. G., Magnani, L., & Rickard, L. J 1986, ApJ, 306, L101
York, H. W., Tenorio-Tagle, G., & Bodenheimer, P. 1983, A&A, 127, 313